ÉCOLE POLYTECHNIQUE
FÉDÉRALE DE LAUSANNE
École polytechnique fédérale de Lausanne (EPFL)

Faculté des sciences de base
Section de physique

Centre de Recherches en Physique des Plasmas (CRPP)

Association EURATOM
Confédération Suisse

Doctoral school

Gamma ray spectrometry in tokamaks

CRPP internal report
INT 212/06

Christian SCHLATTER

PPB 310
CH-1015 Lausanne
Switzerland

2006, 3^d of August, revised on 15th of September.

Made with LaTeX 2$_\varepsilon$

Contents

Chapter 1

Introduction

1.1 Motivation for the use of γ rays to diagnose tokamak plasmas

Knowledge of the behavior of the fusion products is crucial for the understanding of their confinement in future tokamaks, as they are supposed to heat the plasma fuel and to sustain fusion reactions. Extensive studies of the physics of α particles, produced in $D-T$ and $D-^3He$ plasmas were carried out recently.
γ-ray diagnostics were developed and used in these experiments, since the γ-ray photons are inseparably linked to the ongoing nuclear reactions (and the fusion energy production). Most performing γ-diagnostics are currently installed on JET and provide measurements of the energy spectrum and spatial location of various nuclear reactions among plasma fuel ions or with intrinsic impurities and are therefore highly relevant for ITER and beyond. γ-ray spectrometry is currently the unique diagnostic for fusion plasma with nuclear reactions in which no neutrons are produced, whereas in $D-D$ or $D-T$ plasma, this diagnostic scheme complements the capabilities of neutron diagnostics.

Further there is a need for diagnosing different fast ion species simultaneously. In ITER, $D-T$ fusion α's (3.5 MeV) and 1 MeV D-NBI ions need to be detected distinguishably in order to optimize the various plasma scenarios and to acquire extended understanding of fast-ion confinement effects, which is perfectly possible by employing γ ray measurements.

1.2 History of gamma ray measurements in tokamaks

Use of γ-ray emission as a diagnostic tool was already thought of in the late 70's of last century, first measurements were carried out on Doublet-III in 1984, JET followed 1989 and also TFTR and JT60U were equipped with γ-ray diagnostics. Early experimental observations concentrated on nuclear reactions among the plasma fuel constituents. After establishment of the necessary reaction cross sections, also reactions with intrinsic impurities were considered. Not only fusion products but also highly energetic ions injected with neutral beams or accelerated through resonance with ICRF waves produce γ rays upon inelastic collisions with other particles.

Chapter 2

Production of gamma rays in tokamaks

Gamma rays are energetic (> 10 keV) electromagnetic radiations produced by radioactive decay or other nuclear or subatomic processes. Although of the same nature, hard X-rays and gamma rays are termed due to their different origin: the first are due to energetic electron processes, the latter are produced by transitions within the atomic nuclei.

Two sources of gamma rays are commonly distinguished

- gamma rays following beta decay and
- gamma rays following nuclear reactions

In the frame of fusion devices, for the purpose of plasma diagnostic, only the second source of gamma rays is of interest and discussed here. They are one of the final products of two-body initial state nuclear reactions.

Two reaction types are further distinguished:

- Direct production of γ's in nuclear reactions like

$$d + {}^{3}_{2}He \rightarrow \gamma + {}^{5}_{3}Li \tag{2.1}$$

  or

- in two step reactions, often between a low-Z ion (for example: α-particle) colliding with a high-Z (impurity) atom, leaving the atom in an excited state and whose de-excitation gives rise to a gamma-ray photon of characteristic energy, as for example:

$${}^{4}_{2}\alpha + {}^{9}_{4}Be \rightarrow {}^{12}_{6}C^{*} + {}^{1}_{0}n \tag{2.2}$$

The energy of the gamma rays are fixed by energy and momentum conservation of above reactions. The distributions of the reactants peak at energies well below the peak of the reaction cross section (for the direct reaction type, two step reactions exhibit have resonances in the cross section), which is similar to the probability to penetrate the quantum mechanical Coulomb barrier. The reactivity $< \sigma v >$ peaks therefore at intermediate energies. For thermal reactants, the energy of maximum reactivity is given by the Gamow peak,

$$E_G = \sqrt[3]{\pi \alpha Z_1 Z_2 kT} \left(\frac{M_1 M_2}{M_1 + M_2} \right)^{1/3} \tag{2.3}$$

where Z_i and M_i are the charge and mass of the reactants respectively. For non-thermal plasmas the integral $< \sigma v >$ has to be calculated appropriately.

Chapter 3

Diagnostic schemes for gamma rays in fusion devices

The severe environment of a nuclear device requires detectors to be resistant to high neutron fluxes and ability to differentiate the large zoology of possible gamma-ray producing nuclear reactions from neutron induced γ's (produced in by the interaction of the neutrons with the wall and structure materials of the tokamak). High energy resolution, high detection efficiency (for the detection of fast features throughout a discharge) and capability to sustain high count rates are required as well. Only one type of detectors currently fulfills these requirements: scintillators. Some attempts to use semiconductor (mainly germanium) based technology were done in the past, but, although of better energy resolution (due to the direct collection of the charge within the detector) no fusion device employs them so far. The main reasons are the small active volume limited by fabrication (limited detection efficiency), higher cost per volume and increased vulnerability for neutron damage.
Scintillators convert the incident γ's into electrons (to make them visible for detection) and during slowing down of the latter, produce a light pulse which is converted into an electric signal using photomultiplier tubes. Slowing down of the free electrons is achieved within a nanosecond and the electrical pulse is roughly proportional to the energy deposited within the detector.

3.1 Inorganic scintillation materials for γ-ray detectors

The following materials were and are mainly used:

- NaI(Tl): crystalline sodium iodide with traces of thallium iodide. Highest available fluorescent scintillation light yield. First application in 1948, still very suitable and popular. Almost linear energy response (figure 3.1). Decay of scintillation pulse is as fast as 230 ns. A drawback of NaI(Tl) is its afterglow at high counting rates due to phosphorescence.

- Cs(Tl): crystalline Cesium iodide has a better full-energy peak efficiency (see the following section) than NaI(Tl), but at high counting rates its applicability comes to nothing due to the quite long decay time of about 1 ms.

- Bismuth germanate ($Bi_4Ge_3O_{12}$, abbreviated BGO). High density and high-Z (Bi: $Z = 83$) scintillation crystal, largest probability for photoelectric absorption (see below) of available scintillation materials with low afterglow. Very good energy resolution at the price of bad light yield (less than 10 % of NaI(Tl)), timing resolution worse by a factor of two, costs up to the triple of NaI.

For all scintillation materials, the light yield and the scintillation pulse decay time decrease with temperature.

New heavy scintillation materials with better performances than NaI(Tl) were recently developed, but no tests for the radiation hardness and sensitivity to neutrons have been carried out yet.

3.2 Interaction of γ rays with scintillation materials

In order to understand the shape of γ-ray spectra, some knowledge of the interaction with the scintillation materials is necessary. The absorbing matter is ionized via three main processes (relevant for radiation measurements):

- **Photoelectric effect**: Through interaction with an atom, the energy of the photon is transferred to an electron from the atom, which is ejected from the bound shell (most tightly bound K shell, if the energy of the gamma is sufficient). The photoelectron's energy is equal to the energy of the gamma minus the binding energy of the photon. This process is dominating for $E_\gamma < 50$ keV and is enhanced for high-Z absorber. The photoelectric absorption cross section exhibits absorption edges at energies of the gamma corresponding to the binding energy of the electrons in the absorber (see figure 3.1). Photoelectric absorption is the ideal process for measuring the energy spectrum of γ's (the energy of the photoelectron is equal to the energy of the incident gamma minus the binding energy of the electron).

- **Compton scattering**: Interaction between gamma ray and electron in the absorber, which partially absorbs the energy of the gamma and the remaining energy is re-emitted as a new photon with a different angle than the incident photon. As a function of the scattering angle, the incident gamma energy is shared between the recoil electron and the secondary photon, i.e. a wide continuum in photon energy is obtained (see formula 10-2 in Knoll). The maximum energy which can be transferred to the electron is reached in the head-on collision (scattering angle $\theta = \pi$, formula 10-4 in Knoll), which is below the incident gamma energy. At high gamma-ray energies, forward scattering dominates. Compton scattering is the principal absorption mechanism for intermediate energies (100 keV .. 10 MeV). Compton scattering is almost independent of the atomic number of the absorber.

- **Pair production**: The energy of the incident gamma, passing close to the nucleus, is spontaneously converted into mass of a electron-positron pair if its energy exceeds 1.02 MeV (twice the rest mass of the electron). Nevertheless its probability remains low for gamma energies below several megaelectronvolts. Energy in excess appears as kinetic energy shared by the pair. Positron and electron travel a few millimeters before they loose their kinetic energy (within a very short time) to the absorber, then the positron annihilates. Subsequently, the entire mass of the pair is then converted into two annihilation photons of 0.51 MeV each. The importance of this mechanism strongly increases with energy and, as most of the nuclear reactions of interest in tokamaks produce γ's in the range of MeV, is therefore the dominant process.

Figure 3.1.a illustrates these three processes for the range of γ energies above 10 keV for NaI(Tl).

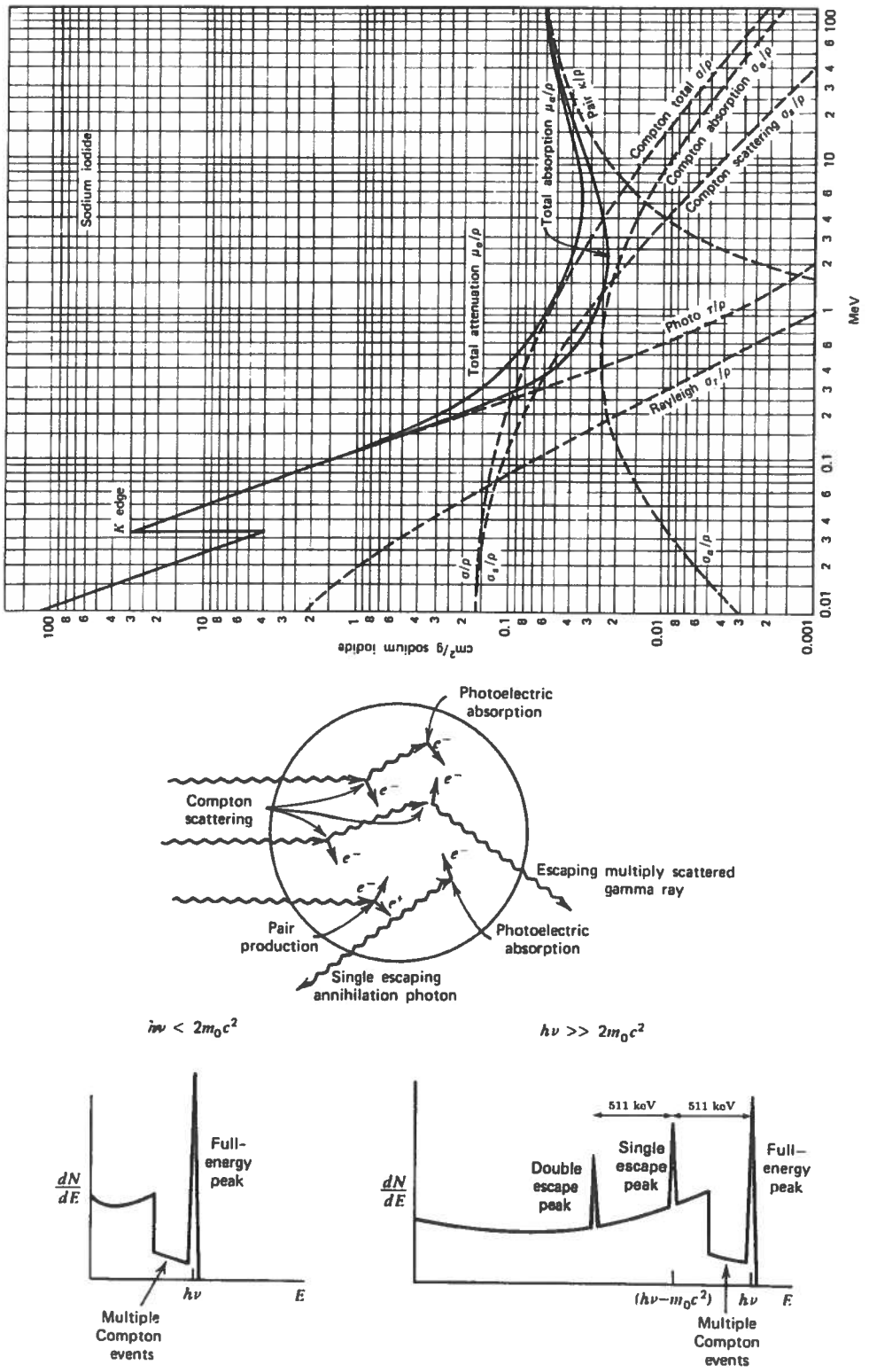

Figure 3.1: a. (top) Energy dependence of the various γ-ray interaction processes in NaI.
b. (bottom) Illustration of the processes for γ-ray detection in a real detector (top). The left plot shows the gap between the Compton continuum and the full-energy peak filled with multiple Compton events followed by photon escape. In the right plot, single and double escape peaks correspond to escape of one or both annihilation photons. Both figures are taken from Radiation, Detection and Measurement by G.F.Knoll, 1989.

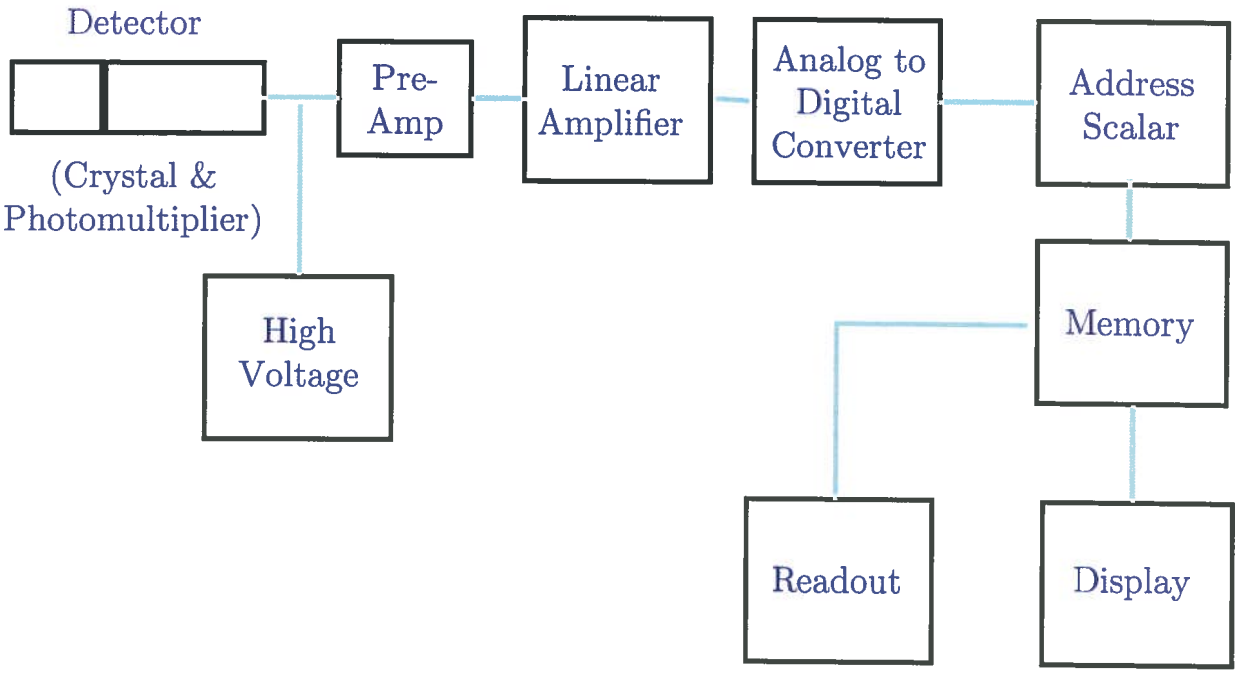

Figure 3.2: Schematic of a multi-channel analyzer.

If the scintillator is large, large in the sense that all secondary radiations (Compton γ's, annihilation photons, even any subsequent generations of these interactions) interact within the detector, then a single pulse, the sum of the response to all electrons produced along the history, is produced (the so-called full-energy peak or photopeak). The detector response is essentially the same as if the incident gamma would have undergone a single photoelectric absorption at once. For typical applications, such a detector would be as large as 10 cm - too large for the requirements in fusion. For typically sized detectors, the detector response looks more complicated. Scattered γ's escape from the detector (Compton continuum with Compton edge), one or both annihilation γ's can escape as well (Single SE or Double escape DE peak at an energy $E = m_0c^2$ or $E = 2m_0c^2$ below the full energy peak), or multiple Compton events without complete deposition of the primary γ energy can partially fill the gap between the Compton edge and the photopeak, see figure 3.1.b.

3.3 Detection electronics

Standard electronics include a high voltage power supply for the photomultiplier bias voltage, the signal output of the photomultiplier tube is amplified with preamplifiers and linear amplifier for pulse shaping, digitized and sorted into an energy spectrum using a pulse height analyzer (PHA) combined with a multi channel analyzer (MCA). Up-to-date electronics like those implemented at JET permit sampling rates of 25 MHz, 14-bit amplitude resolution at a maximum pulse rate of 1 MHz, like the PCI transient recorders currently installed at JET. With the help of software, pulse pile-up can successfully be prevented up to sampling rates of 200 MHz. PHA is possible at counting rates above 10 MHz.

Chapter 4

Brief review of gamma ray detectors installed on tokamaks

Gamma ray detectors in fusion devices have to measure gamma's resulting from different types of nuclear reactions within the plasma, with good discrimination against a strong background of neutrons and neutron induced gamma's (produced through interactions of neutrons with the reactor wall and structure materials). Sophisticated shielding is therefore indispensable. In the following, type, dimensions, details about shielding and utilization of detectors used on tokamaks are shortly reviewed.

4.1 Doublet-III

Sodium Iodide NaI(Tl) crystal (5 cm in diameter, 5 cm long), viewed by a photomultiplier, surrounded by a lead collimator. The detector has a tangential view, 4 m from center.

4.2 TFTR

NaI(Tl) crystal scintillator, 10 cm size, for γ background measurements and liquid fluorocarbon scintillator NE226 (12.7 cm long, diameter) detectors, in sandwich housing (2x2x1m wide, long, high) made of concrete, polyethylene, lead and lithium carbonate). Collimators are 1.5 m long and 20 cm wide. NE226 is insensitive to neutrons, has a rapid decay constant of 2 ns. Measurements of γ's are available up to energies as high as 19 MeV.

4.3 JT60-U

NaI(Tl) scintillator with 50 cm polyethylene and 30 cm lead shield.

4.4 JET

JET has two independent γ-ray diagnostics for the determination of the energy spectra and for the location of the emission.

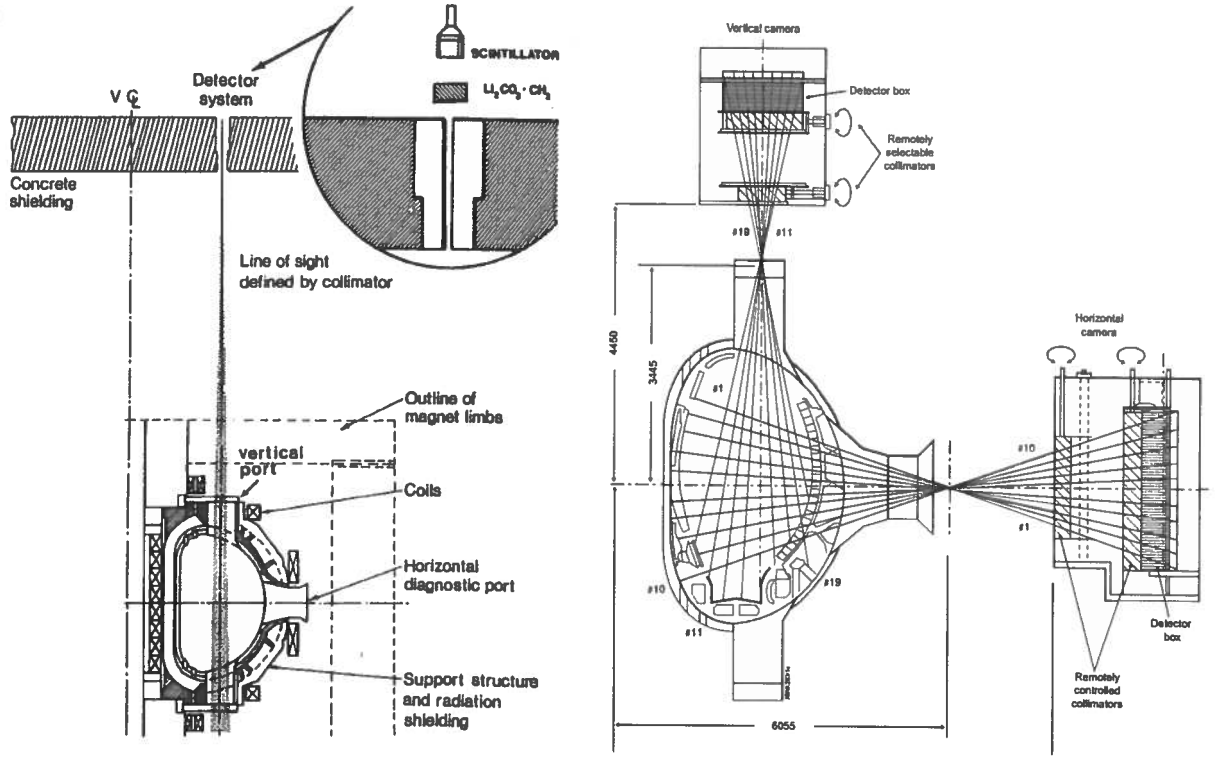

Figure 4.1: a) γ-ray detector with vertical line-of-sight used for the first γ spectroscopy measurements on JET. b) Neutron camera suitable for gamma ray measurements.

4.4.1 energy spectrum (scintillation detectors)

- a horizontal, tangential device (30 cm below magnetic axis) equipped with a bismuth germanate (BGO) scintillation detector (75mm diameter, height). The detector is shielded against neutrons (γ-background, hard X-rays) with polythene (before and behind) and lead (behind the detector, prevents backscattered radiation from penetrating the detector). The energy spectra range from 1 to 28 MeV.

- a vertical device (watching the plasma centre, at $R = 2.9$m) with NaI(Tl) scintillator of 125mm diameter and 150mm height, shown in figure 4.1.a.

The systematic error bar on the detection efficiencies (limited by the geometry and the absorber materials in the line of sight) is < 30 %. Energy calibration is done using standard γ-ray sources. First experiments were carried out in 1987 to estimate the power multiplication factor Q in discharges with 6 MW ICRF tuned to the ^3He minority in D plasma.
As an example, figure 4.2 shows the emission lines of 8 of the 9 first excited states of ^{14}N of resulting from the reaction $^{12}C(^3He, p\gamma)^{14}N$. Knowing the individual cross sections and the relative line intensities, the detailed ^3He distribution function could be reconstructed in principle (see further discussion in the next chapter).

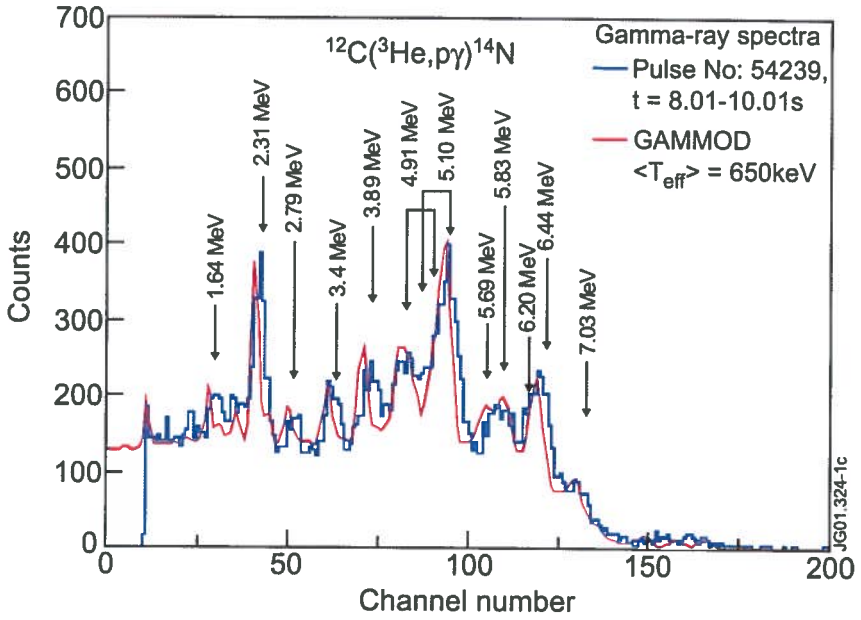

Figure 4.2: γ-ray emission produced by $^{12}C(^3He,p\gamma)^{14}N$.

4.4.2 radial profiles (neutron/gamma camera)

Spatial γ-ray measurements are performed using JET's neutron profile monitor, which was installed in 1996 and which is equipped with two cameras of 9 vertical and 10 horizontal lines of sight (figure 4.1.b). The detectors are NE213 liquid scintillators. γ-ray measurements are possible in ICRF-only heated plasmas by the fact the neutrons and γ's exhibit different pulse shapes (criterion: count rates of γ's and neutrons must be compatible). The energy range of detectable γ's is $E = 1.8..6$ MeV (limited by the pulse-shape discrimination electronics). ICRF+NBI combined discharges are more difficult to analyze due to the strong γ-background level due to neutrons interacting with the walls.

A conclusive proof ensuring that γ's are emitted by the plasma and not by the walls is the observation of individual sawtoothing channels of the Gamma Cameras with inverted sawteeth period at the outer channels and strong signals in the center upon sawtooth crashes.

Since 2005, γ-profiles for energies > 1 MeV are measured using the new diagnostic for fast-electron Bremsstrahlung, incorporated into the neutron profile monitors. An array of 19 CsI(Tl) photo-diodes (10x10x15 mm), remotely placable infront of the neutron detectors with count rate acquisition in four energy windows permits to count specific peaks in the spectrum separately. Calibration is implemented in situ with radioactive sources ^{22}Na. The CsI detector response function was simulated with a Monte Carlo code, its size is suitable for γ detection up to the MeV range and the detector efficiency sufficient for reliable counting.

Chapter 5

Diagnostic performance of gamma rays at JET

In JET, reactants of nuclear reactions producing γ ray radiation are fast ions (produced by fusion, ICRF (some MeV) or NBI (<160 keV)) on fuel ions (H, D, T, ^3He, ^4He) or intrinsic impurities (beryllium, boron, carbon, oxygen) in concentrations below 10 %.
Measured γ ray spectra on JET generally have the shape as presented in section 3.2 with distinct lines due to the interaction of fast ions with low-Z impurities (mainly beryllium) plus a continuum due to the interaction of neutrons with the materials surrounding the plasma (neutron radiative capture).

NBI injected ions are of too low energy to have a direct production of γ rays, but they boost the typical fusion reactions by beam-beam or beam-plasma interactions.
ICRF driven ions reach kinetic energies in the MeV range and inelastically scatter impurity nuclei, for example hydrogen on ^{12}C. The reaction $^{12}C(p,p^*\gamma)^{13}C$ excites the first energy level of the carbon for proton energies above a threshold of 5 MeV (to surmount the Coulomb barrier) and the second level for energies exceeding 8 MeV. Upon return to lower energy levels, γ's with energies corresponding to the transition 4.44 $\rightarrow$ 0 MeV and 7.65 $\rightarrow$ 4.44 MeV (emission of 3.21 MeV γ's) are emitted respectively (figure 5.1). Such thresholds are an important diagnostic feature, when γ's corresponding to these transitions are observed, ions

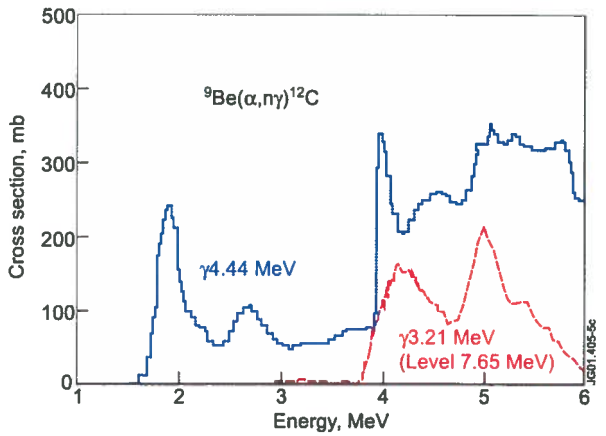

Figure 5.1: Cross section of nuclear reaction $^9Be(\alpha,n\gamma)^{12}C$ for first and second level excitation of the final nucleus.

with energies exceeding these thresholds must necessarily exist within the plasma.

Another diagnostic feature results from resonant capture reactions like $^9Be(p,\gamma)^{10}Be$ with (multiple) γ lines at distinct fast proton energies whose line intensities have the convenient property of being proportional to the fast ion density (the beryllium density is estimated to be uniform and given by spectroscopic measurements).

The combination of NBI and ICRF heating schemes complicates the analysis of the spectra, which is facilitated with the aid of modeling of the gamma-ray emission. For JET, the code GAMMOD was developed, including cross section for all nuclear reactions producing γ's observed so far, shown in table 5.1

The code tries to reproduce the γ background, line positions, intensities and widening. GAMMOD assumes Maxwellian fast ion distribution functions for bulk and tails for ICRF accelerated ions and classical slowing down expressions for NBI and fusion born ions. GAMMOD assesses effective fast ion tail temperatures by fitting the width of the Gamow peaks (including the Doppler broadening) with error bars below 30%. Figure 5.2.b shows an example of experimental and modeled γ ray spectra.

5.1 Popular nuclear reactions with diagnostic benefit for gamma ray spectroscopy

5.1.1 Scenarios with ICRF tuned to hydrogenic minorities

In JET's tritium campaign (~90 % concentration of T), the hydrogen minority (~5 %) was accelerated with ICRF. In figure 5.2.a the hot protons (of energy > the threshold of ~5 MeV) are clearly visible through $^{12}C(p,p^*\gamma)^{12}C$, whose peak width was used to estimate a tail temperature of ~400 keV, in agreement with JET's high energy neutral particle analyzer KF1. The presence of fast protons is in agreement with the neutron diagnostics, which measure 40 % excess neutrons through $T(p,n)^3He$. Important to note that there is no acceleration of deuterons (although present by ~5 % of the plasma density and the second harmonic resonance of D coincides with the fundamental resonance of H), since the emission of the previously discussed reaction $^{12}C(d,\gamma)^{13}C$ is absent in the spectrum.

In contrast, several fast ion species can be accelerated simultaneously by ICRF and identified on the γ spectrum. ICRF acceleration of D in deuterium discharges, again tuned to the hydrogen minority, is clearly visible in figure 5.2.b.

5.1.2 Scenarios with ICRF tuned to ^3He minorities

In deuterium plasmas with a concentration of about ~20 % of ^3He with ICRF at $\omega_{^3He}$, RF power damping on D and ^3He is observed (figure 5.3.a) through reactions $^{12}C(d,p\gamma)^{13}C$ and $D(^3He,\gamma)^5Li$ respectively.

Fast protons are observed as well (again through $^{12}C(p,p^*\gamma)^{12}C$), whose population is most likely created through the fusion reaction $D(^3He,p)^4He$. The 17 MeV γ emission is routinely used to measure the ICRF power deposition efficiency.

Reaction	Energy of reaction, Q (MeV)	E_{min} (MeV)[a]
Protons		
$D(p,\gamma)^3He$	5.5	0.05
$T(p,\gamma)^4He$	19.81	0.05
$^9Be(p,p'\gamma)^9Be$	−2.43	3
$^9Be(p,\gamma)^{10}B$	6.59	0.3
$^9Be(p,\alpha\gamma)^6Li$	2.125	2.5
$^{12}C(p,p'\gamma)^{12}C$	−4.44, −7.65	5, 8
Deuterons		
$^9Be(d,p\gamma)^{10}Be$	4.59	0.5
$^9Be(d,n\gamma)^{10}B$	4.36	0.5
$^{12}C(d,p\gamma)^{13}C$	2.72	0.9
Tritons		
$D(t,\gamma)^5He$	16.63	0.02
$^9Be(t,n\gamma)^{11}B$	9.56	0.5
^3He *ions*		
$D(^3He,\gamma)^5Li$	16.38	0.1
$^9Be(^3He,n\gamma)^{11}C$	7.56	0.9
$^9Be(^3He,p\gamma)^{11}B$	10.32	0.9
$^9Be(^3He,d\gamma)^{10}B$	1.09	0.9
$^{12}C(^3He,p\gamma)^{14}N$	4.78	1.3
Alphas		
$^9Be(^4He,n\gamma)^{12}C$	5.70	1.9

Table 5.1: Nuclear reactions identified in γ-ray spectra recorded at JET.

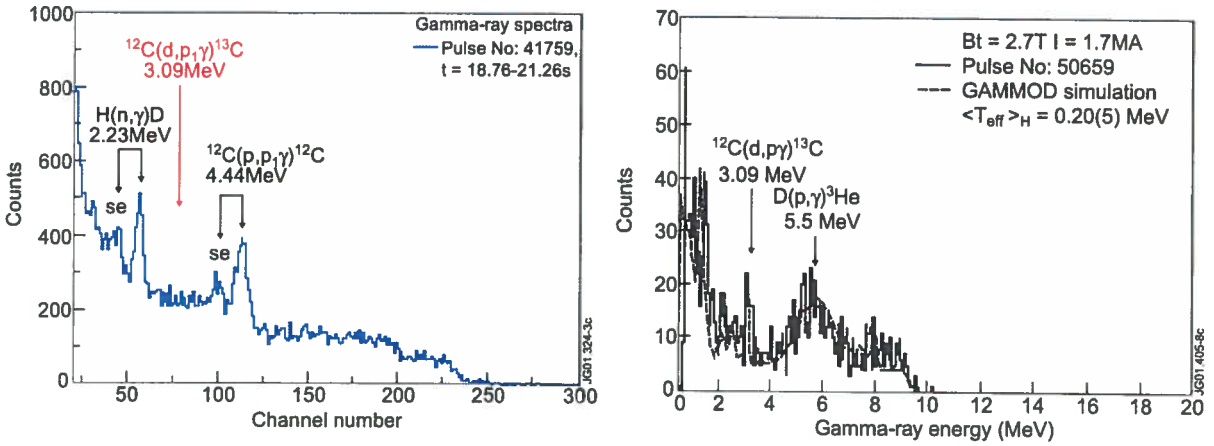

Figure 5.2: a. (left) Tritium plasma with hydrogen minority heating. No indication for the presence of fast deuterium.
b. (right) Deuterium plasma with yydrogen minority heating. Experimental and modeled γ-ray spectra.

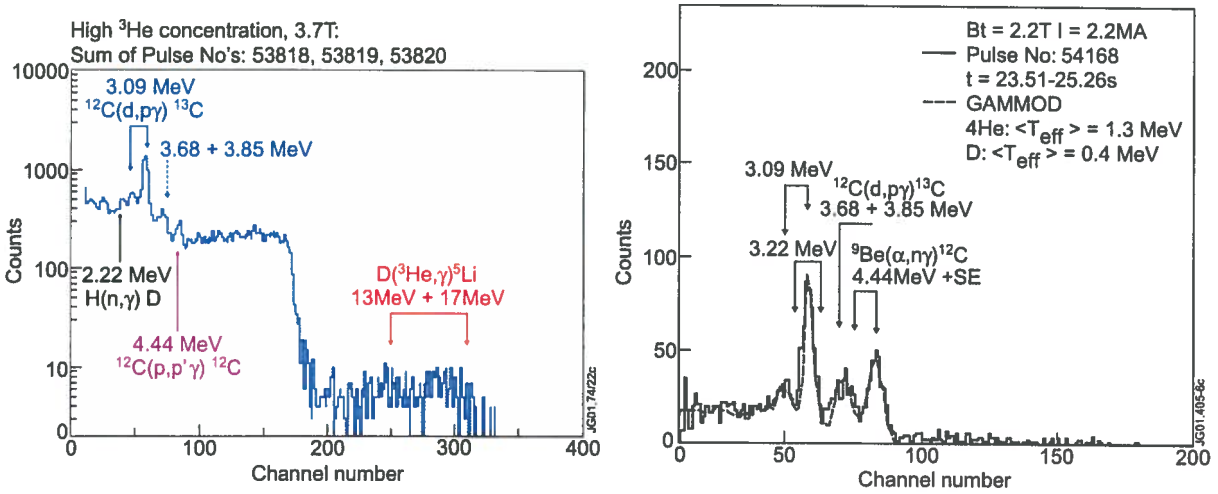

Figure 5.3: a. (left) 20 % ^3He plasma with ICRF tuned to the ^3He cyclotron frequency. The ICRF power is damped on hydrogen and deuterium.
b. (right) ^4He plasma. ICRF induced acceleration of D and neutral beam ^4He with third harmonic heating of both species.

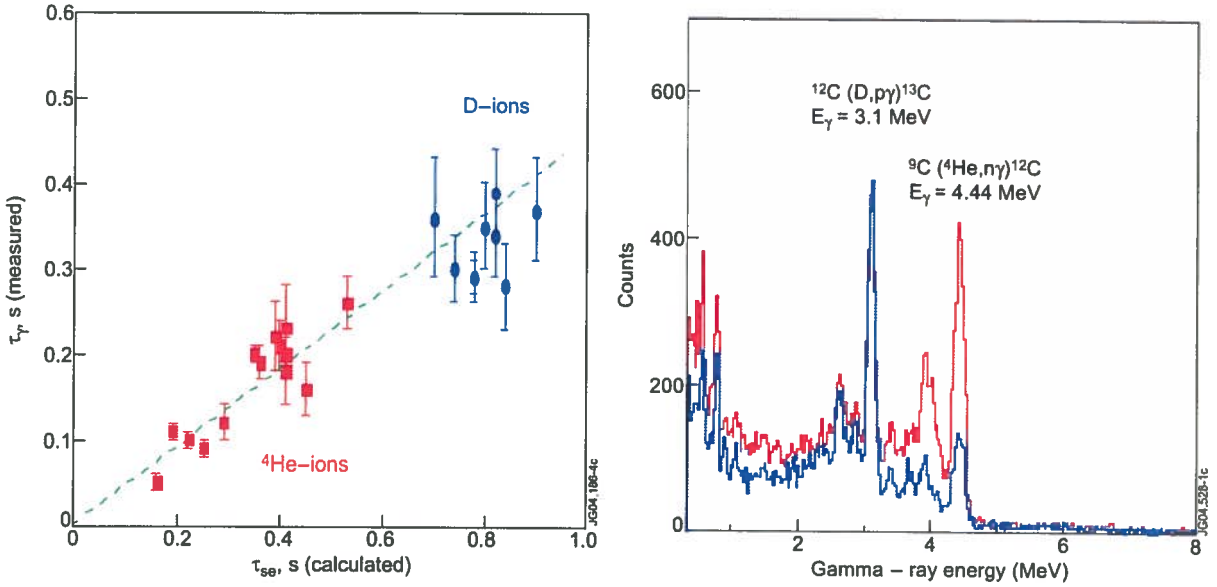

Figure 5.4: a. (left) Relationship between γ-ray decay time and classical relaxation of ICRF accelerated particles were obtained by modulating the RF power.
b. (right) Effect of reaction thresholds: When the NBI energy is decreased from 110 keV (red) to 70 keV (blue), the second energy level of ^{12}C is much less excited.

5.1.3 Scenarios with ICRF accelerated ^4He beam and fusion born α's

Helium plasmas have the advantage of being accompanied by a low neutron yield, but if some % of the ICRF power are absorbed by hydrogenic species, strong neutron yield can appear. In ^4He plasmas with ^4He NBI ($\leqslant$ 100 keV) and resonant heating at $\omega = 3\omega_{^4He} = 3\omega_D$ fast D and further accelerated ^4He beam ions ($^9Be(\alpha, n\gamma)^{12}C$, exceeding 2 MeV) are observed (figure 5.3.b).

With pulsed ICRF power the relaxation of the fast particles was studied using the vertical γ ray detector. The γ ray decay times are about half (possibly due to changes in T_e after RF power level modification) the classical slowing down time (but scale correctly as $\sim A/Z^2$) of both species (figure 5.4.a).

With lower energy (but constant power) of the ^4He beam, the ICRH absorbtion decreases and γ emission as well, see figure 5.4.b.
The same nuclear reaction with beryllium was used to diagnose fusion born α particles in the trace tritium campaign (tritium seeding with NBI blips, figure 5.5). The excitation of the second energy level of the final nucleus ^{12}C (requires α's exceeding 4 MeV) is only seen during the blip (γ emission at 3.2 MeV, figure 5.6).
In contrast to the experiment with ICRF accelerated ^4He, the plasma conditions could be kept constant after the blip and the γ ray decay times are in agreement with the confinement and classical slowing down time of the α particles in scenarios without non-classical particle losses.

Presently there is no possibility to determine the velocity-decomposition in parallel and perpendicular directions in respect to the magnetic field (no distinction between trapped and passing ions).

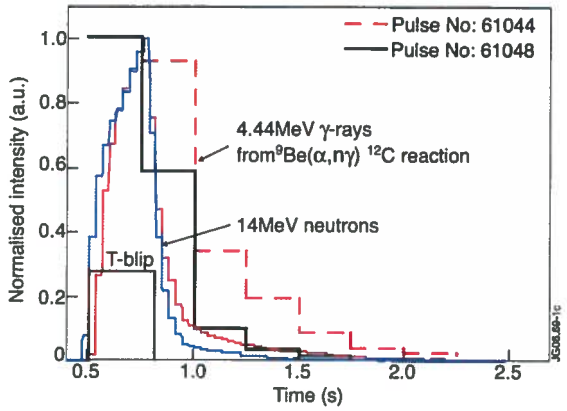

Figure 5.5: a. (left) Relaxation of NBI deposited tritium as seen by neutron and γ-ray diagnostics.

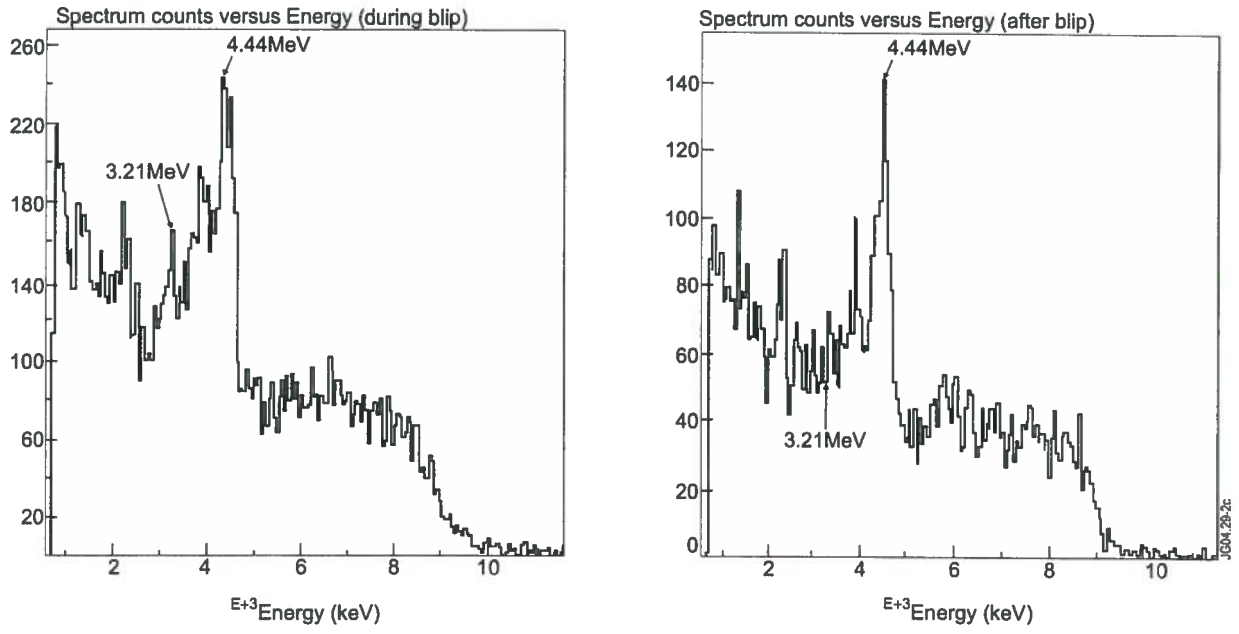

Figure 5.6: γ-ray emission during and after the tritium blip.

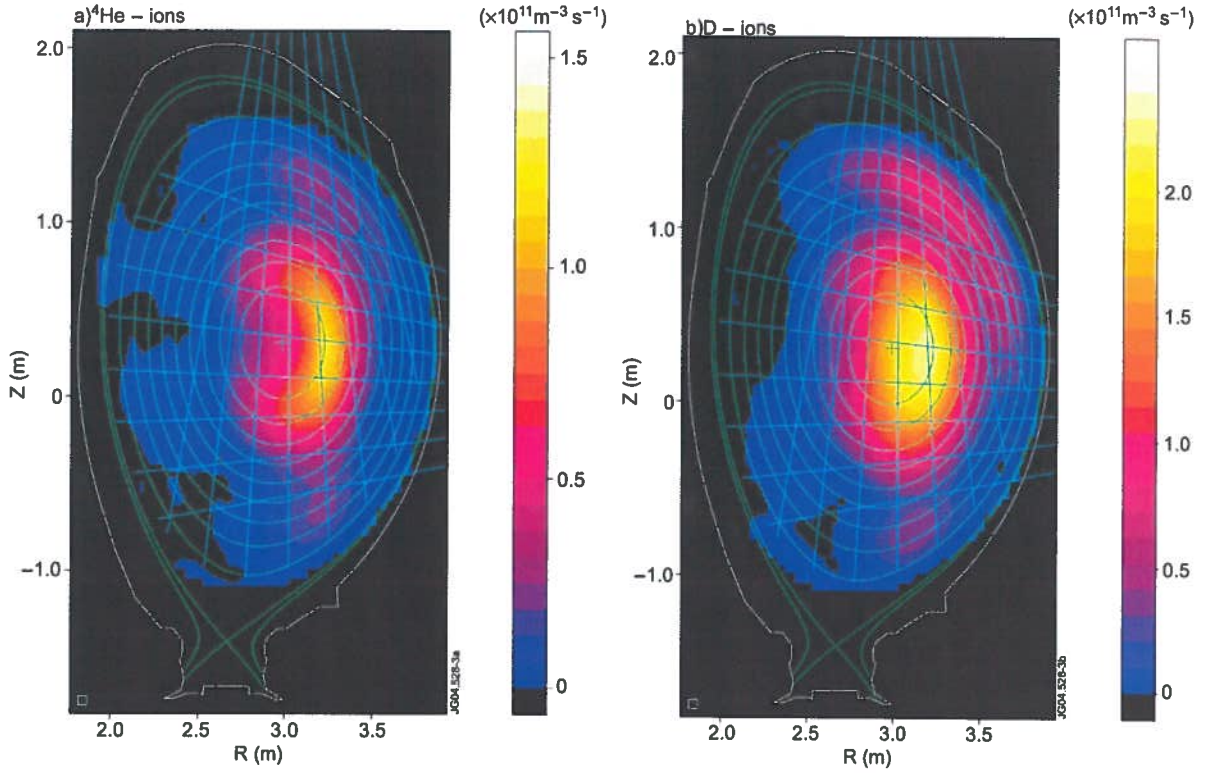

Figure 5.7: Reconstructed γ-ray profiles of 4.44 MeV (left, $^9Be(\alpha, n\gamma)^{12}C$) and 3.09 MeV (right, $^{12}C(d, p\gamma)^{13}C$) γ-ray emission.

5.2 Gamma ray tomography

Gamma emission measurements with the neutron cameras were successfully reconstructed tomographically, unfolding the spatial distribution of the fast ions. A grid based constrained optimization method that uses anisotropic smoothness on flux surfaces as regularization, featuring a non-negativity constraint, is used for the inversion. The geometry of detectors and collimators are taken into account, attenuation or scattering of γ's on their flight towards detectors are not. The spatial resolution is about 6 cm.
The tomographic reconstruction of a poloidal section depicted in figure 5.7 shows the differences in pitch angle distribution of ICRF heated D (isotropic) and NBI (tangentially) injected (and ICRF heated) ^4He ions in a ^4He plasma. The γ emission was simultaneously recorded in energy windows containing full energy, single energy and double energy peaks of γ's emitted by nuclear reactions involving D and ^4He separately, during a steady state time interval of 1 s.
Another example are advanced regime plasmas with Alfvén cascades and reversed shear sawtooth instabilities (therefore non-monotonic q-profile), where very broad ^4He banana orbits are expected. With monotonic q-profiles, the orbits are smaller (figure 5.8).

5.3 Further improvements of γ ray diagnostics in JET

Spectrometers with higher energy resolution could better resolve the Doppler-broadening of the γ-ray lines. γ profile measurements require averaging over a steady-state phase of the discharge, currently the efficiency of the available detectors and their neutron rejection capability are not good enough to make time-resolved measurements. Employment of better detectors (see next chapter) in a multi chord camera would offer the possibility to achieve 3D γ measurements (in energy *and* space)...

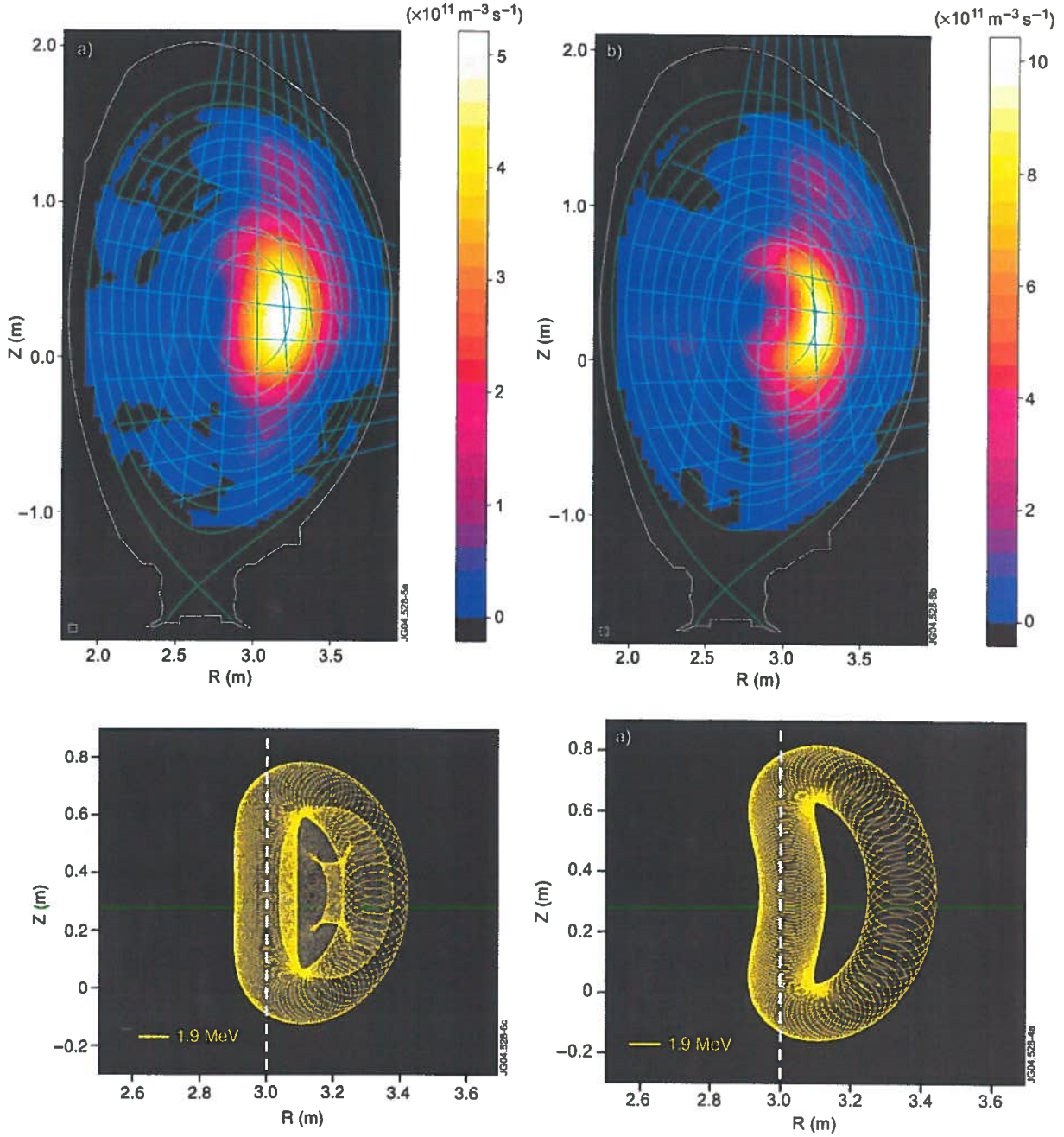

Figure 5.8: Reconstructed γ-ray profiles of 4.44 MeV γ's from $^9Be(\alpha, n\gamma)^{12}C$ with non-monotonic (top left) and monotonic (top right) q-profiles. The calculated corresponding ^4He ion orbits are shown below.

Chapter 6

Plans for ITER

α-particle diagnosis is planned to take place through $D(t,\gamma)^5He$ and $^9Be(\alpha,n\gamma)^{12}C$ (E_γ = 4.44 MeV), as beryllium will probably be the main impurity in ITER. γ ray cameras similar to those currently exploited on JET could measure 3.5 MeV α birth profiles (17 MeV γ rays) and confined α-particle slowing down up to 1.7 MeV (through 4.4 MeV γ's). Slowing down of deuterons could be measured through $^9Be(d,n\gamma)^{10}Be$ and $^9Be(d,p\gamma)^{10}Be$ (E_γ = 2.88 and 3.37 MeV respectively).
Time resolved profile measurements require highly efficient spectrometers with sufficient neutron background rejection (peak-to-background ratio). GAMMACELL (figure 6.1.b) was developed for this purpose, whose detector array functions as full-energy absorption spectrometer (9 Ba_2F scintillators which are highly radiation resistant) for E = 1-30 MeV. ^6LiH acts as neutron filter and was successfully tested on JT-60U (the gamma-background was reduced by one order of magnitude).

The current design of ITER plans to incorporate the gamma cameras into the ITER neutron cameras with adjustable collimators for the collimation and neutron suppression required for the experiment.

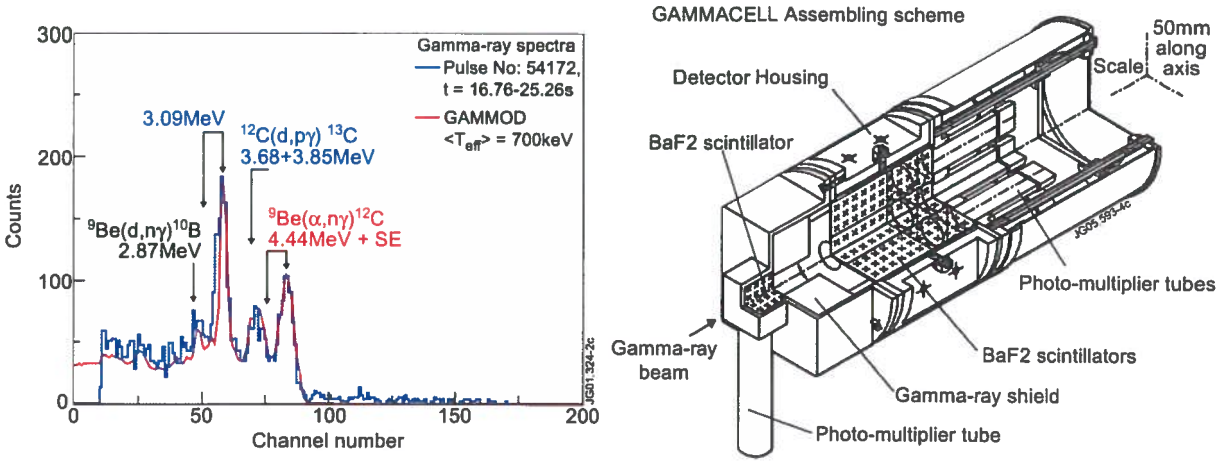

Figure 6.1: a) Nuclear reactions involving beryllium.
b) Advanced γ-ray detector for fusion plasmas GAMMACELL.

Chapter 7

Bibliography

The most exhaustive bibliography of γ-ray spectroscopy emphasizing the work carried out at JET can be found in the preprint paper EFDA-JET-PR(05)38 written by V.G.Kiptily, F.E.Cecil and S.S.Medley, to be published in Plasma Physics and Controlled Fusion.

Concerning the principles of γ-ray detectors and scintillations materials, see Glenn F. Knoll, Radiation, Detection and Measurement, New York, 2000.